ARTICLE

Check for updates

Large characteristic lengths in 3D chiral elastic metamaterials

Tobias Frenzel [1,2,6], Vincent Hahn[1,2,3,6], Patrick Ziemke[2,3,6], Jonathan Ludwig Günter Schneider[1], Yi Chen[1], Pascal Kiefer [1,2], Peter Gumbsch[2,3,4,5] & Martin Wegener[1,2,3 ✉]

Three-dimensional (3D) chiral mechanical metamaterials enable behaviors not accessible in ordinary materials. In particular, a coupling between displacements and rotations can occur, which is symmetry-forbidden without chirality. In this work, we solve three open challenges of chiral metamaterials. First, we provide a simple analytical model, which we use to rationalize the design of the chiral characteristic length. Second, using rapid multi-photon multi-focus 3D laser microprinting, we manufacture samples with more than 10^5 micrometer-sized 3D chiral unit cells. This number surpasses previous work by more than two orders of magnitude. Third, using analytical and numerical modeling, we realize chiral characteristic lengths of the order of ten unit cells, changing the sample-size dependence qualitatively and quantitatively. In the small-sample limit, the twist per axial strain is initially proportional to the sample side length, reaching a maximum at the characteristic length. In the thermodynamic limit, the twist per axial strain is proportional to the square of the characteristic length. We show that chiral micropolar continuum elasticity can reproduce this behavior.

[1] Institute of Applied Physics (APH), Karlsruhe Institute of Technology (KIT), 76128 Karlsruhe, Germany. [2] 3DMM2O-Cluster of Excellence (EXC-2082/1-390761711), Karlsruhe Institute of Technology (KIT), 76128 Karlsruhe, Germany. [3] Institute of Nanotechnology (INT), Karlsruhe Institute of Technology (KIT), 76128 Karlsruhe, Germany. [4] Institute of Applied Materials - Computational Materials Science (IAM-CMS), Karlsruhe Institute of Technology (KIT), 76128 Karlsruhe, Germany. [5] Fraunhofer Institute for Mechanics of Materials (IWM), 79108 Freiburg, Germany. [6] These authors contributed equally: Tobias Frenzel, Vincent Hahn, Patrick Ziemke. ✉email: martin.wegener@kit.edu

In ordinary elastic bulk solids, twist effects are of lesser importance than strains, or they are absent altogether. For example, transverse (TA) and longitudinal (LA) acoustic phonons appear in all bulk solids, whereas additional twist acoustic modes only appear in elastic achiral or chiral beams with finite cross-section[1]. As another example, the classical rank-four Cauchy elasticity tensor describes the generally rich connection between strains and stresses, whereas it completely neglects chiral twist effects. This asymmetry between strains and twists in elasticity is related to the fact that twist effects depend on the sample size. More specifically, in three-dimensional (3D) crystalline materials or metamaterials composed of a total of $N_x \times N_y \times N_z$ unit cells with $N_x \propto N_y \propto N_z \propto N$, the integer number N is decisive. In sharp contrast, usual strain-related effects do not depend on N.

On this background, our 2017 experiments on pronounced push-to-twist conversion effects in chiral architectures came as somewhat of a surprise[2] (also see refs. [3,4]). In these experiments[2], we demonstrated large static twist effects in 3D cubic chiral metamaterials composed of moderately large total numbers of cubic unit cells of ≤500. We experimentally found a slow but monotonous decrease of the twist angle per axial strain, $\varphi(N)/\epsilon_{zz}$ at predescribed ϵ_{zz}, when increasing N from 1…5 for a fixed sample height-to-width aspect ratio of $A = 2$. For larger N, the computed asymptotic decrease followed the beam's surface-to-volume-ratio $\propto 1/N$. Later, the unit cell suggested in ref. [2] was systematically optimized in the sense of maximizing $\varphi(1)/\epsilon_{zz}$ for a single unit cell by using topology optimization[5].

Three more recent independent conceptual studies[6–8], loosely based on ref. [9], aimed toward systematically modifying and improving the qualitative and quantitative behavior of $\varphi(N)$ with $N \gg 1$ for metamaterial crystals composed of many unit cells. The results presented in refs. [6,7], both show that the behavior of twist versus N can be tailored by the coupling strength between chiral unit cells. In ref. [7], early model experiments on corresponding samples with a macroscale unit-cell size of $a_{xy} = 2.4$ cm, fabricated by macroscopic 3D printing, were reported as well.

On the level of effective continuum descriptions, the behavior of $\varphi(N)$ has been described by generalized elasticity, e.g. by Eringen[10] and Lakes[11]. Therein, several chiral and achiral characteristic length scales are defined. Different characteristic length scales for one metamaterial have also previously been discussed for two-dimensional achiral elastic metamaterials[12,13]. There, analytical expressions were derived[12], relating the length scales to geometrical parameters of the microstructure. In the context of chiral 3D periodic elastic metamaterials, characteristic length scales have previously been discussed in generalized continuum theories beyond Cauchy elasticity, such as micropolar Eringen elasticity[2,11] or Willis elasticity[14]. These length scales[2,9] have been comparable to or even smaller than the unit cell size, or lattice constant, of the metamaterial crystal.

In the present paper, building on previous studies[2,6], we design a feasible 3D tetragonal metamaterial crystal unit cell. We manufacture corresponding 3D metamaterial samples with a microscale unit cell size of $a_{xy} = 74$ μm and $a_{xy} = 150$ μm, respectively, characterize them under uniaxial compression, and compare the experimental results of the twist angle φ versus N to numerical calculations, to micropolar continuum elasticity following Eringen[10], and to a simple analytical model. Within this model, the twist angle at fixed strain ϵ_{zz} and fixed sample height-to-width aspect ratio A linearly increases with N up to a certain maximum characteristic number N_c. Upon multiplication of N_c with the unit cell size, we obtain the characteristic length L_c. Beyond that maximum at $N = N_c$, the twist angle asymptotically decreases as $\propto 1/N$. We reproduce this behavior by micropolar continuum elasticity. In our experiments, we achieve characteristic lengths

that are on the order of ten times the unit cell size. This progress allows for much larger twist effects than previously[2] for a total number of unit cells in the metamaterial >10^5—which has to be compared to <10^3 in previous works[2,9]. Thereby, this work brings twist effects closer to applications. One possible application is to combine such chiral metamaterials with a linear piezoelectric actuator, enabling to convert the actuator motion into a rotation (also cf. [15]). There, overall millimeter-sized metamaterial crystals exhibiting large twist effects are desirable.

Results

Simple analytical model. Figure 1 shows the blueprint of the 3D chiral unit cell that we consider in this paper. This tetragonal cell is placed on a tetragonal translation lattice with lattice constants $a_x = a_y \neq a_z$. The unit cell is composed of only a single simply connected constituent material and voids within (vacuum or air). The colors are for illustration only. The blue cubic part is intentionally identical to the cubic unit cell discussed in our earlier work[2], therefore allowing for a direct comparison. As previously[2], the indicated angle δ allows to control the degree of chirality. For $\delta = 0$, the unit cell becomes achiral and twist effects are zero by symmetry. The red parts shown in Fig. 1 are the crucial novelty of the present paper with respect to ref. [2]. These connectors determine how the twist angle builds up from a single unit cell to a 3D crystal (see right of Fig. 2a). This 3D
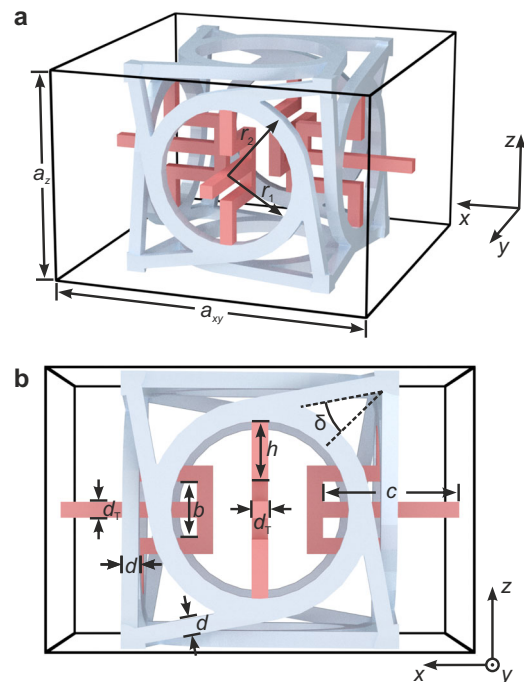
Fig. 1 Illustration of one unit cell of the chiral tetragonal mechanical metamaterial considered here. a, b Different viewing directions. All are made from one material, the colors are for illustration only. Within the xy-plane, adjacent unit cells are connected only by the red arms of length $2c$ and width d_T. In the z-direction, the unit cells are connected directly. The blue cubic part in the middle is identical to that in ref. [2] with radii r_1, r_2, and angle δ of the arms with respect to the cubic face diagonal. A non-zero δ makes the unit cell chiral. This tetragonal unit cell with lattice constants $a_x = a_y = a_{xy} = 74$ μm or $a_{xy} = 150$ μm (depending on the fabrication technique) and $a_z = (2/3) \times a_{xy}$ is placed on a tetragonal translation lattice. Further geometrical parameters used throughout this paper are: $r_1/a_{xy} = 21.3\%$, $r_2/a_{xy} = 26.7\%$, $b/a_{xy} = 14.2\%$, $c/a_{xy} = 34.2\%$, $d/a_{xy} = d_T/a_{xy} = 4\%$, $h/a_{xy} = 14.2\%$, $\delta = 34.8°$.
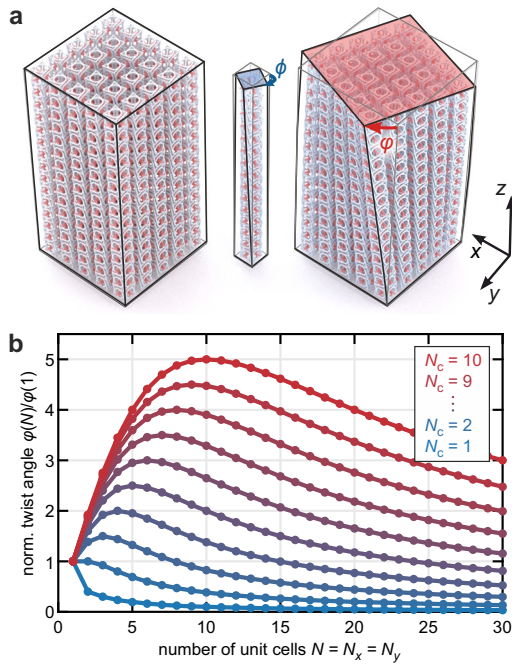
Fig. 2 Illustration of the simple analytical model. a Crystal lattices composed of $N_x \times N_y \times N_z = 5 \times 5 \times 15$ (left and right) and $1 \times 1 \times 15$ (center) unit cells of the type shown in Fig. 1. Under compressive loading, the $1 \times 1 \times 15$ column twists by the indicated angle $\phi = \varphi(1, 15) < 0$. The metamaterial crystal to the right twists under compressive loading by the indicated mean angle $\varphi = \varphi(5) = \varphi(5, 15) < 0$, which is generally different from ϕ. The difference of the two angles, mediated by the red connector arms (also see Fig. 1), leads to an important contribution to the total linear-elastic energy within the simple model. **b** Calculated twist angles $\varphi(N) = \varphi(N, 3N)$ from our simple analytical model versus integer values of N (dots) for different characteristic numbers $N_c = 1, 2, ...10$ (see legend). The straight lines between dots are merely guides to the eye. For $N_c > 1$, $\varphi(N) / \varphi(1)$ monotonously increases as a function of N and reaches its maximum at N_c. For $N > N_c$, the twist angle approaches an $\propto 1/N$ decay.

metamaterial crystal is composed of a total of $N_x \times N_y \times N_z$ unit cells with the choices $N = N_x = N_y$ and $N_z = 3N_x = 3N$ (see left of Fig. 2a).

In the following simple model, we consider the twist angle $\varphi(N_x, N_z)$ which results from the predetermined axial compressive strain ϵ_{zz} within the linear elastic regime. We use traction-free boundary conditions for the four beam side faces and no external torques are applied. Edge effects are neglected. For $N_x = 1$, the twist angle $\phi = \varphi(1, N_z)$ can be seen as a "microtwist". For $N_x > 1$, $\varphi(N_x, N_z)$ is the twist angle of the overall metamaterial beam or the "macrotwist". For fixed predetermined axial strain ϵ_{zz}, the twist angle of a single unit cell, $\varphi(1, 1)$, is fixed and proportional to ϵ_{zz}. This angle $\varphi(1, 1)$ is an input parameter of the model. For stapling $N_z > 1$ unit cells along the z-direction, the individual twist angles simply add up, i.e.,

$$\varphi(1, N_z) = N_z \varphi(1, 1). \tag{1}$$

Likewise, for stapling entire xy-planes of N_x^2 unit cells, the mean twist angles also add up

$$\varphi(N_x, N_z) = N_z \varphi(N_x, 1). \tag{2}$$

We consider three contributions to the linear elastic energy:

$$W = W_1 + W_2 + W_3. \tag{3}$$

The first term, W_1, is the usual compression energy given by

$$W_1 = c_1 N_x^2 N_z \epsilon_{zz}^2, \tag{4}$$

with coefficient c_1. For simplicity, we have neglected the strains in the directions other than the z-direction, which is a good approximation if the effective Poisson's ratio, v, is small, $|v| \ll 1$. This condition is fulfilled for the architecture shown in Figs. 1 and 2a for loading along the z-direction. If the Poisson's ratio should not be close to zero, the other strain components are proportional to ϵ_{zz} in the linear elastic regime. Hence, the other energy contributions can effectively be lumped into a renormalized coefficient c_1 and the general form of the first term W_1 stays the same. In any case, the contribution W_1 does not enter directly into the resulting twist angle.

The second term, W_2, is the twist energy of a (chiral or achiral) metamaterial beam, which is given by

$$W_2 = c_2 \frac{N_x^4}{N_z} \varphi(N_x, N_z)^2, \tag{5}$$

with coefficient c_2 (ref. [16]).

The third term, W_3, starts from the fact that the twist angle of a single unit cell, $\varphi(1, 1)$, is generally different from that of an xy-plane of unit cells, i.e., $\varphi(1, 1) \neq \varphi(N_x, 1)$. That is, if a single unit cell alone wants to twist by the microtwist $\varphi(1, 1)$ but the xy-plane twists by $\varphi(N_x, 1)$, an elastic energy $c_3 (\varphi(N_x, 1) - \varphi(1, 1))^2$, with coefficient c_3, results for each unit cell. Multiplication with the total number of unit cells $N_x^2 N_z$ in the metamaterial beam leads us to

$$W_3 = c_3 N_x^2 N_z (\varphi(N_x, 1) - \varphi(1, 1))^2 = c_3 \frac{N_x^2}{N_z} (\varphi(N_x, N_z) - \varphi(1, N_z))^2. \tag{6}$$

The resulting macrotwist angle $\varphi(N_x, N_z)$ for fixed ϵ_{zz} is obtained from the minimum of the elastic energy W, i.e., from the condition

$$\frac{\partial W}{\partial \varphi(N_x, N_z)} = 0. \tag{7}$$

With the definition for the characteristic number N_c,

$$N_c^2 = c_3/c_2, \tag{8}$$

with the choice $N_z = 3N_y = 3N_x = 3N$ as used in the below experiments (also see Fig. 2a), and using the shorter nomenclature $\varphi(N) = \varphi(N, 3N)$, which is possible for fixed sample height-to-width aspect ratio A, we obtain

$$\varphi(N>1) = \varphi(1) \frac{N N_c^2}{N^2 + N_c^2}. \tag{9}$$

The behavior of $\varphi(N)$ is determined by only two parameters. As introduced above, the parameter $\varphi(1) = 3\varphi(1, 1)$ is given by the twist angle of a single unit cell $\varphi(1, 1)$ for a given axial strain ϵ_{zz} in the linear elastic regime. $\varphi(1)$ is obviously a property of an individual unit cell and not a property of how the unit cells are connected to a 3D crystal. The fit parameter N_c describes the effects resulting from the coupling of the cells in the x- and y-directions. N_c determines the shape of $\varphi(N)$ versus N, whereas $\varphi(1)$ is merely a prefactor. Exemplary curves of $\varphi(N)$ for different values of $N_c = 1, 2, ..., 10$ are depicted in Fig. 2b. For $N_c \gg 1$, the function $\varphi(N)$ starts $\propto N$ for $N \ll N_c$, exhibits a maximum at $N = N_c$, and asymptotically decays $\propto 1/N$ for $N \gg N_c$. For $N_c \approx 1$ or even < 1, no maximum occurs any more for integer values $N = 1, 2, ...,$ and we rather obtain a monotonous decrease of $\varphi(N)$ versus N, as in our previous work[2]. A direct comparison of $\varphi(N)/\epsilon_{zz}$ from the simple analytical model with microstructure-based simulations

and micropolar continuum theory will be given in the "Discussion" section alongside the experiments.

Microstructure-based simulations. In the unit cell illustrated in Fig. 1, the characteristic number N_c is tailored by the red elongated rods of total length $2c$ and width d. To make the metamaterial unit cell compact, we have retracted the starting points of these elongated rods to the inside of the cubic blue part via the red "U"-shaped parts. In sharp contrast, the unit cells are connected without any intermediate element along the z-direction. This direct connection favors that the twist angle builds up linearly from one end of the metamaterial beam to the other. It is this wanted asymmetry between the z-direction and the xy-directions which makes the unit cell shown in Fig. 1 tetragonal rather than cubic. Our choice of the dimensions of the red parts are the result of a trade-off. If we left away the red parts (or give them zero stiffness), we would get $c_3 = 0$, but also $c_2 = 0$, leaving N_c undefined. If we replaced the red parts by a very much stiffer material than the blue parts, c_3 would increase, but c_2 would become very large, too[6].

To evaluate whether 3D metamaterial crystals based on the 3D unit cell design depicted in Fig. 1 behave as expected from the simple analytical model outlined in the preceding section, we have performed finite-element numerical calculations. In a first approach, we have employed the standard finite-element software package Comsol (MUMPS solver). The used geometrical parameters are given in the caption of Fig. 1 and the parameters of the single constituent material are given in the "Methods" section. We fix the sample bottom and attach a plate at the top of the sample where we apply an uniaxial compression along the z-direction with prescribed displacement u_z, and use traction-free boundary conditions for the four sample side faces. The twist angle φ is computed from the displacements of the corners of the top plate. The axial strain is defined by $\epsilon_{zz} = u_z/L_z$. We choose a sample height-to-width aspect ratio of $A = L_z/L_x = L_z/L_y = 2$. Together with the chosen lattice constants of $a_x = a_y = a_{xy}$ and $a_z = (2/3) \times a_{xy}$, this leads to $N_z = 3 \times N_x$ and $N_x = N_y = N$. Thus, the total number of unit cells in a metamaterial crystal with aspect ratio A and integer N is given by $(a_x/a_z)AN^3 = 3N^3$. For the constituent material, we use a Young's modulus of $E = 2.6$ GPa, and Poisson's ratio of $\nu = 0.4$. The obtained numerical results for $N \leq 6$ (648 unit cells total) will be discussed and compared to our experiments below.

In our above discussion of the simple model, we have briefly mentioned the Poisson's ratio. Therefore, we present numerically calculated Poisson's ratios in Supplementary Fig. S1. Indeed, the Poisson's ratios are close to zero.

However, our below experiments extend to integer values N as large as $N = 27$. Using the described continuum finite-element approach, values much larger than 6 are presently out of reach due to computational constraints. To obtain at least some qualitative theoretical guidance based on the metamaterial microstructure, we radically simplify the architecture shown in Fig. 1 by using Timoshenko beam elements. Details are described in the "Methods" section and Supplementary Fig. S2. By using roughly 2.2×10^6 beam elements, we have obtained convergent results for a total number of up to 24,000 unit cells ($N = 20$ and $A = 2$), while accounting for geometrical nonlinearities. It should be noted though that the Timoshenko beam approach grossly underestimates the effective Young's modulus of the metamaterial. This aspect is expected because slender beams are a bad approximation for the regions in Fig. 1 where the arms merge into the rings, leading to a stiffening of these regions. However, the effective Young's modulus does not directly enter into the observable $\varphi(N)/\epsilon_{zz}$ versus N that we focus on in this paper.
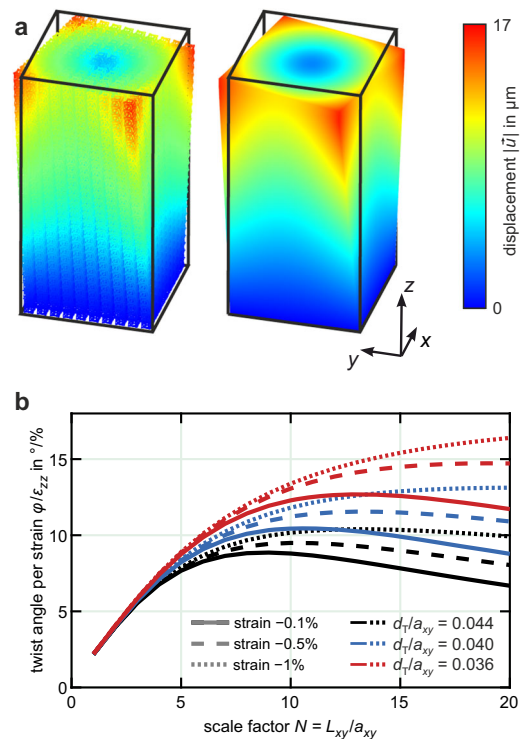
Fig. 3 Numerical calculations of the twist behavior. a Calculated behavior of a metamaterial beam as shown in Fig. 1 under compressive loading along the axial (z) direction. Left: Microstructure Timoshenko beam calculation for $N = 10$ ($3N^3 = 3000$ unit cells total), $\epsilon_{zz} = -0.1\%$, $d_T/a_{xy} = 4.4\%$, and $a_{xy} = 150 \, \mu m$. Right: Calculation based on linear micropolar Eringen continuum elasticity (for parameters, see Supplementary Note 1). For clarity, all displacements are exaggerated by a factor of 15. The actual displacements are given by the false-color scale. **b** Derived twist per strain φ/ϵ_{zz} versus N for three different Timoshenko beam diameters d_T and for three different axial strains ϵ_{zz} (see legend). For clarity, we have drawn continuous curves versus N, while only data at integer values of N have been calculated. The behavior can be compared to that of the simple model shown in Fig. 2b. To allow for a direct comparison with the experimental and with other theoretical data, the three black curves are reproduced in Fig. 5.

An example of calculated raw data from the Timoshenko beam approach within the linear elastic regime for $N = 10$ is depicted on the left-hand side of Fig. 3a. In Fig. 3b, we show the calculated $\varphi(N)/\epsilon_{zz}$ versus N for three different compressive axial strains and for three different beam diameters, d_T, corresponding to the red beams in Fig. 1. The diameter of $d_T = 0.04 \times a_{xy} \approx 3 \, \mu m$ roughly mimics the parameters given in Fig. 1. The two other diameters d_T depicted in Fig. 3b are different by merely about $\pm 10\%$, equivalent to about $\pm 0.3 \, \mu m$ for one of the later used lattice constant of $a_{xy} = 74 \, \mu m$. Two trends can be seen. First, for small strains of $\epsilon_{zz} = -0.1\%$ toward the linear elastic regime, the behavior in Fig. 3b depends very sensitively on the beam diameter d_T. As expected from our above qualitative discussion, thinner (thicker) beams lead to a larger (smaller) position of the maximum of $\varphi(N)/\epsilon_{zz}$ versus N, hence of the characteristic number N_c. However, the magnitude of the dependence on d_T is obviously quite pronounced. The characteristic number changes likewise when changing the beam stiffness by changing its length c at otherwise fixed parameters. The corresponding behavior is depicted in Supplementary Fig. S3. Second, for all three d_T, we find a pronounced dependence of $\varphi(N)/\epsilon_{zz}$ on the magnitude of the compressive axial strain when going from $\epsilon_{zz} = -0.1\%$ via

−0.5% to −1.0%. Pronounced geometrical nonlinearities are apparent, even for small strains $|\epsilon_{zz}| < 1\%$. This aspect has been discussed previously[6] and we will come back to it in our discussion and comparison with experiments.

Micropolar continuum elasticity. The mapping of the metamaterial structure behavior onto an effective continuum description is important to us because it can be argued[17] that calling a metamaterial a "material" requires that its properties can be mapped onto a suitable continuum description, containing effective material parameters that do not depend on size or conditions, but that are rather material specific. To avoid misunderstandings, we emphasize that such mapping does not imply by any means that we are able to determine the effective parameters uniquely ("parameter retrieval"). A unique effective parameter retrieval would necessitate to consider a large number of dissimilar deformation modes of the structure, which is well beyond the scope of this paper.

In brief, in micropolar elasticity[10], the rank-two strain tensor $\overleftrightarrow{\epsilon}$ and the rank-two curvature tensor $\overleftrightarrow{\kappa}$ are connected to the rank-two stress tensor $\overleftrightarrow{\sigma}$ and couple stress tensor $\overleftrightarrow{m}$ via the four rank-four tensors $\overleftrightarrow{A}$, $\overleftrightarrow{B}$, $\overleftrightarrow{C}$, and $\overleftrightarrow{D}$. The tensors $\overleftrightarrow{B}$ and $\overleftrightarrow{D}$ are connected[10]. In components and using the Einstein summation convention, we have

$$\sigma_{ij} = \frac{\partial w}{\partial \epsilon_{ij}} = C_{ijkl}\epsilon_{kl} + D_{ijkl}\kappa_{kl}, \quad (10)$$

$$m_{ij} = \frac{\partial w}{\partial \kappa_{ji}} = A_{jikl}\kappa_{kl} + D_{klji}\epsilon_{kl}, \quad (11)$$

with elastic energy density w. Note the order of subscript indices in A_{jikl} and D_{klji}. The reciprocity condition imposes the following major symmetries onto C_{ijkl} and A_{ijkl}[10],

$$C_{ijkl} = C_{klij}, \quad A_{ijkl} = A_{klij}. \quad (12)$$

For the tetragonal crystal symmetry of interest in this paper, these four elasticity tensors can be parameterized by a total of 29 different non-zero scalar parameters. As explained in ref. [18] for the case of a cubic crystal, these parameters are connected via the condition that the elastic energy w must be positive for passive materials. Following along the lines of ref. [19], we arrive at a first guess for these parameters. Next, we numerically post-optimize them by a trial-and-error procedure. The resulting set of nonzero effective material parameters (see Supplementary Note 1) corresponds to the lattice constant of $a_{xy} = 150\,\mu m$, $a_z = 100\,\mu m$, a constituent material Young's modulus of $E = 2.6$ GPa, and a Poisson's ratio of $\nu = 0.4$. An example calculation is shown on the right-hand side of Fig. 3a. It can be compared directly to the Timoshenko beam microstructure calculation on the left-hand side of Fig. 3a. The overall deformation of the metamaterial beam is well grasped by micropolar continuum elasticity. Numerical results for $\varphi(N)/\epsilon_{zz}$ versus N in the linear elastic regime are shown and compared to other data in the "Discussion" section.

Experiments. We have manufactured a large set of 3D chiral tetragonal microstructured metamaterials, including samples containing a very large number of unit cells by an approach that we have published recently[20]. This approach is based on multiphoton polymerization of a monomer photoresist, using a 3×3 array of laser foci instead of just a single focus, rapid scanning of the laser foci with a peak velocity of $0.4\,ms^{-1}$, leading to a total peak printing rate of about 10^7 voxels s^{-1}, and tight focusing of all femtosecond laser pulses by a microscope lens with a numerical aperture of NA = 1.4. With this setup, the total

printing time (including all overheads and settling times) for the $N = 27$ sample, which contains a total of $2 \times 3 \times (27)^3 = 118,098 > 10^5$ unit cells, is about 30 h. Obviously, this setup only allows for values of N that are integer multiples of 3. For details of this home-built setup, we refer the reader to ref. [20] and the "Methods" section. For these samples, we have used the commercial photoresist IP-Dip (Nanoscribe GmbH), as in our previous work using this multi-focus setup[20].

For the making of smaller samples with $N = 1...6$, we have used the same commercial 3D laser printer (Photonic Professional GT, Nanoscribe GmbH) as in our original work[2,21,22]. The lateral lattice constant for theses samples is $a_x = a_y = a_{xy} = 150\,\mu m$. With this setup, the printing time for the $N = 6$ sample is about 19 h. For these samples, we have used the commercial photoresist IP-S (Nanoscribe GmbH), as in our original work[2]. In this manner, we also compare results of two different constituent materials. The constituent material properties are expected to drop out for the quasi-static twist angle per axial strain, φ/ϵ_{zz}[11], which we will focus on in the "Discussion" section.

To avoid the need for sliding boundary conditions at the sample top, as previously[2], we fabricate and characterize a left-handed metamaterial on top of a right-handed metamaterial or vice versa. Therefore, the total torque is zero. Thereby, the middle of the sample twists, whereas the top and the bottom of the sample do not twist. To monitor the twisting of the middle, we add marker areas in the middle of the sample edges. For very large samples, these markers are not necessary, hence we have partly left them away.

Figure 4 exhibits a gallery of electron micrographs of polymer samples with different values of N, revealing generally very high quality. Some of the samples, especially those with large N, are visibly twisted after the fabrication process. We assign this finding to sample shrinkage after the development process. If shrinkage was isotropic, all dimensions would shrink alike and no twist results. However, the mere fact that the metamaterial samples are fixed to the substrate breaks the symmetry. In addition, the slicing and hatching procedure in the 3D printing process (see "Methods" section) makes the polymer structure somewhat anisotropic locally. If, for example, the shrinkage in the axial z-direction was 10% and that in the lateral xy-directions was 9.9%, the relative difference of 1% would effectively act as an axial strain of $\epsilon_{zz} < 0$, leading to sample twist angles on the order of up to 10° according to the mechanism discussed above. A relative asymmetry of 1% in polymer shrinkage is amazingly small and cannot be avoided to our experience. This pre-twist introduces a systematic error to our experimental data, the magnitude of which is difficult to estimate. If the resulting polymer is not pre-stressed after shrinkage, and if one assumes a linear behavior starting from the pre-twisted configuration, the pre-twist has no influence at all. The positive side of this unwanted pre-twist is that its presence already indicates that the aimed-at mechanism for achieving large values of $\varphi(N)/\epsilon_{zz}$ at large integers N works, because similar pre-twists were barely visible in our earlier experiments[2].

Measurement results for $\varphi(N)/\epsilon_{zz}$ versus N for different chosen values of ϵ_{zz} are shown in Fig. 5. For small samples (i.e., $N \le 10$), relatively small strain values are prone to large experimental errors and hence not shown, whereas relatively large strain values are not accessible for large samples (i.e., $N \ge 10$) due to irreversible sample deterioration. These results are further discussed in the following section.

Discussion

In Fig. 5, we summarize our results for the twist angle per axial strain, $\varphi(N)/\epsilon_{zz}$, versus the integer number of unit cells
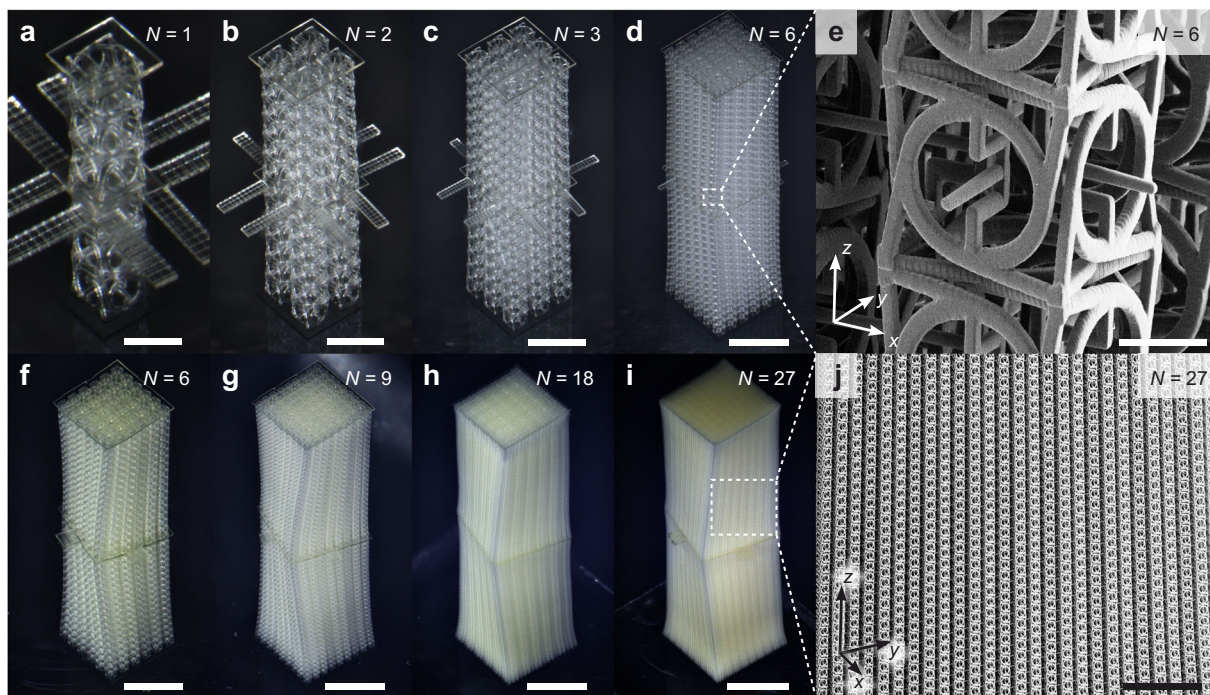
Fig. 4 Gallery of selected polymeric chiral tetragonal mechanical metamaterial samples following the design shown in Fig. 1. a–d Optical micrographs of samples with $N = 1, 2, 3, 6$ fabricated using the Nanoscribe 3D printer. **a** $N = 1$, scale bar: 100 μm. **b** $N = 2$, scale bar: 200 μm. **c** $N = 3$, scale bar 300 μm. **d** $N = 6$, scale bar: 600 μm. **e** Scanning electron micrograph of one unit cell of the sample with $N = 6$ depicted in **d**, scale bar: 40 μm. **f–i** Optical micrographs of samples with $N = 6, 9, 18, 27$ fabricated using the multi-focus multi-photon 3D printer. **f** $N = 6$, scale bar: 300 μm. **g** $N = 9$, scale bar: 450 μm. **h** $N = 18$, scale bar: 900 μm. **i** $N = 27$, scale bar: 1350 μm. **j** Zoomed-in scanning electron micrograph of the sample with $N = 27$ depicted in **i**, scale bar: 300 μm.

$N = N_x = N_y$ and $N_z = 3N$ (hence sample height-to-width aspect ratio $A = 2$) in a chiral tetragonal metamaterial. Five independent data sets are depicted: (1) simple analytical model, (2) continuum finite-element microstructure calculations, (3) Timoshenko beam calculations, (4) Eringen micropolar continuum theory, and (5) experiment. For cases (1) and (3), for clarity and to distinguish from the experimental data points, we have drawn continuous curves versus N, while only the integer values of N are physically meaningful. For Eringen micropolar continuum theory, the depicted continuous curve versus N is meaningful, because N is defined via the sample side length $L_x = 150$ μm according to $N = L_x/a_x = L_y/a_y$, which can assume non-integer values.

First, the data (1)–(5) in Fig. 5 consistently exhibit an initial increase of $\varphi(N)/\epsilon_{zz}$ versus N, followed by a maximum, and a decrease. Achieving this behavior has been the main point of this paper. For the simple analytical model, we fix $\varphi(1)/\epsilon_{zz} = 2.4°/\%$, and depict a range of values for N_c from 7 to 10, leading to a peak twist angle per axial strain around 8–$12°/\%$. This value is about 4–6 times larger than the maximum of $2°/\%$ in ref. [2]. More importantly, in the large-sample limit, for $N \to \infty$, the twist angle per axial strain is $\propto N_c^2$. This leads to a 17–35 fold increase compared to the material in ref. [2]. Values larger than $2°/\%$ are achieved here at integers N as large as $N = 27$, for which the overall fabricated specimen contains a total of $2 \times 3 \times (27)^3 = 118,098$ unit cells, which compares to a total of $500 < 10^3$ unit cells in ref. [2]. The number of 118,098 complex 3D unit cells even surpasses previous record values for mechanical metamaterials[20].

The blue symbols in Fig. 5 correspond to the photoresist IP-S (Nanoscribe GmbH) and $a_{xy} = 150$ μm, the red symbols to the photoresist IP-Dip (Nanoscribe GmbH) and $a_{xy} = 74$ μm. The blue and red data points agree for $N = 3$ and $N = 6$. This behavior confirms the theoretical expectation that, within the linear-elastic regime and for fixed unit-cell shape, $\varphi(N)/\epsilon_{zz}$ should neither depend on the Young's modulus of the constituent material nor on the absolute value of the metamaterial lattice constant a_{xy} (ref. [6]). The reproducibility of different measurements on the same sample can be assessed by comparing different symbols of the same kind and color and brightness at a given N. The reproducibility concerning different nominally identical samples can be seen by comparing the light-red and dark-red symbols, and the light-blue and dark-blue symbols, respectively.

A closer inspection of the data in Fig. 5 shows a strong influence of nonlinearities, even for absolute values of the axial strain significantly below 1% (cf. subsection "Microstructure-based simulations"). These nonlinearities are such that the twist angle per strain increases with increasing absolute values of the axial strain. At first sight, this strain dependence, which is encoded by the different symbols for the experiment, might be misinterpreted as errors or scattering in the experimental data. This general trend was already found in our original work[2], but it was much less pronounced there. Here, this trend is also fairly small at integers smaller than $N \approx 5$. However, it becomes quite prominent at around $N \approx 15$, where the relative changes in twist angle per strain amount to relative 50% and more. The Timoshenko beam calculations (also see Fig. 3b) and the experiments qualitatively agree in regard to this trend, although the nonlinearities appear to be yet more pronounced in the experimental data. The origin of the corresponding quantitative differences between calculations and experiments is presently not clear. We can say, however, that we have not found any indication of irreversible modifications of our samples in the experiments shown in Fig. 5, in which six loading cycles have been performed subsequently. As discussed in subsection "Microstructure-based simulations", we have only accounted for geometrical nonlinearities in the Timoshenko beam calculations. Due to computational limitations, these calculations have only been possible up to $N = 20$, whereas the experimental
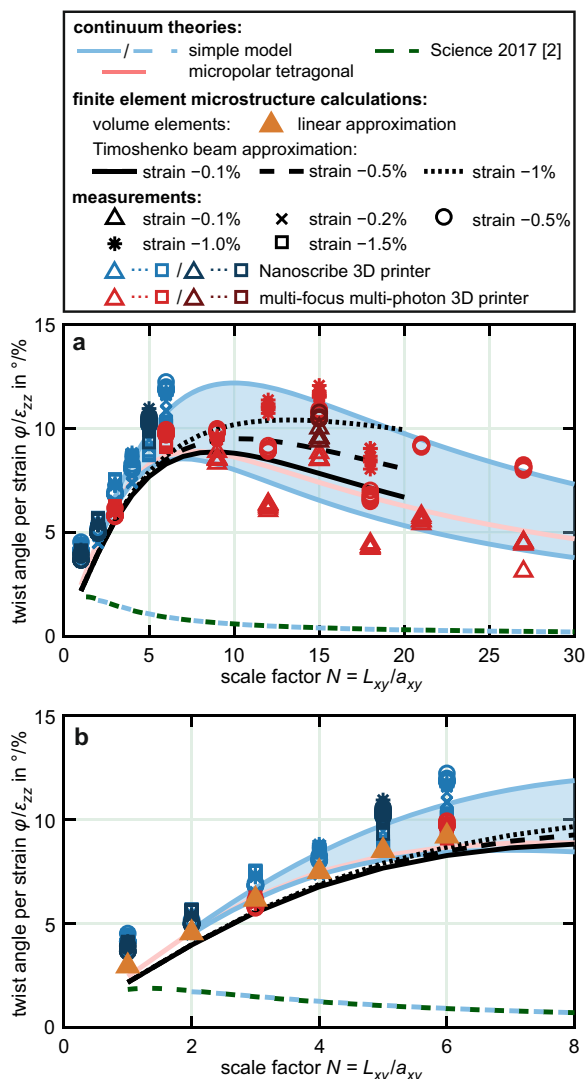
Fig. 5 Summary of the numerical and experimental results of the twist per axial strain. a A metamaterial composed of unit cells as shown in Fig. 1 is subject to an axial compressive strain (cf. Fig. 3a). The resulting twist angle per axial strain, $\varphi(N)/\epsilon_{zz}$, is plotted versus N. For the chosen lattice constants and chosen fixed sample height-to-width aspect ratio of $A = 2$, the resulting total number of metamaterial unit cells is given by $N_x N_y N_z = 3N^3$. In the experiments, the stacking of a left-handed and a right-handed sample part leads to a total number of $N_x N_y N_z = 2 \times 3N^3$. Five types of results are summarized: experiments, microstructure calculations using beam elements (the three black curves are the same as in Fig. 3b for $d_T/a_{xy} = 4.4\%$), micropolar Eringen elasticity computations, and the simple analytical model. For experiment and microstructure calculations, results for different strain values are depicted (see symbols and legend). Dark-red (dark-blue) and light-red (light-blue) symbols at a given N correspond to experiments on different samples. Different measurements on the same sample are also shown. Eringen elasticity and the simple model are within the linear-elastic limit. For the simple model, we depict a range of curves corresponding to fixed $\varphi(1)/\epsilon_{zz} = 2.4°/\%$ and varying N_c from 7 to 10, for the tetragonal case as considered here. For the case of ref. [2], we fit $\varphi(1)/\epsilon_{zz} = 2.0$ and $N_c = 1.7$. **b** Same as **a**, plus microstructure calculations using volume elements and for a smaller range of N to improve the visibility of the large number of data points at small N.

data go up to $N = 27$. We note that the magnitude and the sign of the geometrical nonlinearities are generally different for compressive or tensile axial strain, respectively[6]. The experiments reported here are restricted to compressive strain $\epsilon_{zz} < 0$.

Nonlinearities are neglected in the simple model as well as in linear micropolar elasticity.

Within the linear elastic regime, the simple analytical model, the continuum finite-element calculations, and the Timoshenko beam calculations for an axial strain of $\epsilon_{zz} = -0.1\%$ agree well, indicating that the simple model qualitatively grasps the underlying physics. We recall that the simple model contains only two parameters, of which one, $\varphi(1)/\epsilon_{zz}$, is merely a prefactor and the other one, the characteristic number N_c, solely determines the shape of the curve. Furthermore, linear Eringen micropolar elasticity also agrees well. Here, due to the large number of 29 different non-zero parameters, we are neither in a position to guarantee that we have achieved the best possible fit nor can we claim that our choice is unique. Nevertheless, we can say that we have found a reasonable set of parameters. It should also be stressed again that these 29 parameters are connected via the condition that the corresponding elastic energy needs to be positive definite. The existence of such material parameters appears important to us because it shows that the general behavior can be mapped onto an effective-medium description. In this description, the parameters of the four elasticity tensors are constant and do not depend on the sample size, whereas the behavior depicted in Fig. 5 is obviously very strongly dependent on sample size via the integer N. On this basis, the architectures discussed in this paper qualify as metamaterials in the strict sense[17].

One may have expected that micropolar elasticity, which accounts for local displacements and local rotations, is not sufficient because the red parts of the unit cell in Fig. 1 are additionally deformed (sheared) when applying a compressive axial strain. Micromorphic Eringen elasticity (using nine elasticity tensors) is a generalization of micropolar Eringen elasticity (using four elasticity tensors) and explicitly accounts for such local shear deformations[10]. However, micromorphic Eringen elasticity does not appear to be necessary to understand the complex chiral metamaterial behavior presented here.

Finally, we note that the simple analytical model is not only able to describe the results presented here, but also our original 2017 results on cubic chiral metamaterials[2]. The simple model for the parameters $\varphi(1) = 2.0$ and $N_c = 1.7$ is shown by the green curve at the bottom of Fig. 5. This green dashed curve overlaps within the line thickness with the result of Eringen elasticity for the parameters in ref. [2], which is shown by the light-blue dashed curve. Effective values of N_c in between $N_c = 1.7$ (ref. [2]) and $N_c = 7.2$ (this work) as well as yet larger values could be obtained by varying the thickness d of the red connector arms in Fig. 1, while fixing all other parameters (cf. Fig. 3b and ref. [6]).

Conclusion

Chiral effects of artificial elastic solids called metamaterials have recently emerged, but are not accounted for on the level of classical textbook Cauchy elasticity. This fact is connected to the scale invariance of Cauchy elasticity, which means that it contains no characteristic length. Therefore, the elastic properties do depend on the material, but for a given material they do not depend on the sample size. In contrast, micropolar elasticity following Eringen does account for chiral effects and is not scale invariant. Therefore, certain elastic properties do depend on the sample size. This dependence can be expressed by introducing characteristic lengths, which determine from which point on the asymptotic behavior toward Cauchy elasticity begins.

In this paper, we have discussed a chiral 3D tetragonal mechanical metamaterial architecture that allows for tailoring the chiral characteristic length. In particular, we have shown here that the characteristic length scale can be made much larger than the

metamaterial lattice constant of $a_{xy} = 74\,\mu m$ or $a_{xy} = 150\,\mu m$, respectively. This step brings pronounced chiral effects to metamaterial crystals containing a much larger number of unit cells, $>10^5$, than previously. Corresponding analytical solutions of a simple and intuitive model, numerical volume finite-element calculations for 3D metamaterial microstructures, numerical Timoshenko beam calculations, numerical solutions of chiral micropolar continuum elasticity following Eringen, and extensive experiments on microstructured 3D mechanical metamaterials are in good qualitative agreement.

Methods

Microstructure calculations using volume elements. We utilized the commercial software package COMSOL Multiphysics to perform finite-element calculations of the microstructure. The microstructure was split up into tetrahedral mesh elements (up to 1.2×10^6 elements for $N = 6$). We solved the ordinary Cauchy continuum mechanics equations using quadratic Lagrange shape functions and the MUMPS solver. A linear elastic material with a Young's modulus of 2.6 GPa and a Poisson's ratio of 0.4 was assumed. To reduce the computational effort, only the bottom half of the structure, that is, only one handedness, was simulated. The mimic the experimental boundaries, we fixed all degrees of freedom at the bottom of the structure. As in the experiment, we attached a plate to the top of the structure with outer dimensions of $N_x a_{xy} \times N_y a_{xy} \times 0.1 a_z$. Due to the generally large computational demands of this method, it was not possible to compute structures larger than $N = 6$, equivalent to a total of $6 \times 6 \times 3 \times 6 = 648$ unit cells.

Microstructure calculations using beam elements. As discussed in the main paper, the twist per strain versus N starts with an increase $\propto N$, followed by a maximum, and a decrease $\propto N_c^2/N$. In our proposed structure, the maximum and the decrease occur for $N > 6$, where finite-element calculations of a microstructure meshed with continuum elements become infeasible. To support our findings to beyond $N = 6$, we simplified the structure by using Timoshenko beam elements (cf. Supplementary Fig. S2) and carried out geometrically nonlinear finite-element calculations of samples comprised of up to $N = 20$, equivalent to a total of $20 \times 20 \times 3 \times 20 = 24{,}000$ unit cells. For the simplified microstructure calculations, we used the software ABAQUS 3DEXPERIENCE R2018x and the beam element B32. We assumed a linear elastic behavior of the constituent material with a Young's modulus of 2.6 GPa and a Poisson's ratio of 0.4. We constrained all degrees of freedom at the bottom face of the sample. At the top face, we rigidly coupled all degrees of freedom to a single reference point located in the centroid of the top face. We applied a displacement u_z in the vertical direction to this reference point such that a compressive engineering strain of $\epsilon_{zz} = u_z/L_z = -1\%$ was achieved. On all other surfaces, we applied traction-free boundary conditions. This choice of boundary conditions allowed us to only simulate one half of the samples, and the rotation of the reference point corresponds to the measurements discussed in the "Experiments" section.

A simplified extended unit cell is shown in Supplementary Fig. S1. All red beams of the unit cell have a cross-section of $d_T \times d_T$. All blue beams have a cross-section of $d \times d$, except for those constituting the octagons in the faces of the cube, that simplify the rings of the original unit cell (see Fig. 1). At the side faces, these beams have a cross-section of $d \times d_R$ with $d_R = r_2 - r_1$. In the bottom and the top face of the unit cell, the octagons of neighboring unit cells coincide when they are stacked along the z-axis. For these octagons, instead of defining two coinciding sets of elements and nodes and assigning each element a single beam width, we only defined one set of elements and assigned them double the beam width, leading to a cross-section of $d \times 2d$. Thereby, we used less elements per unit cell and saved computational costs. With this procedure, parts of neighboring unit cells are already included in this extended unit cell. Therefore, when stacking unit cells along the z-axis, either the ring at the bottom or top had to be left away to avoid double counting of theses rings. The ABAQUS model of the unit cell (*.cae file), a python script creating simulation input decks (*.inp files) for different N and all individual input decks used to create the data in the main paper are provided in the repository given in the section on "Data availability".

Sample fabrication. Three modifications of the multi-focus multi-photon 3D printer with respect to that in ref. [20] shall be noted here. First, we installed a motorized aperture in order to blank all but the central laser focus while 3D printing the marker arms attached to the plate located at the middle of the structure. Second, due to changes of one of the telescopes, the focus spacing and hence the lattice constant of the metamaterial is $a_x = a_y = 74\,\mu m$ here (compared to $80\,\mu m$ previously[20]). Third, to make the 3D printer more compact, we have exchanged the prism dispersion-compensation unit. Here, we use only a single highly dispersive N-SF66 prism (instead of two previously[20]), which is Brewster-angle cut for 800 nm wavelength. The beam is back-folded onto this single prism, such that it passes the prism four times[23], leading to an effective tip-tip distance of about 0.9 m (compared to 2 m previously[20]). The hatching distance is set to 200 nm, the slicing distance to 300 nm. We have used the commercial photoresist

IP-Dip (Nanoscribe GmbH) and a 40× objective lens (numerical aperture NA = 1.4, Carl Zeiss).

For the smaller samples printed by the Nanoscribe 3D printer, the hatching distance is set to 300 nm, the slicing distance to 700 nm. We have used the commercial photoresist IP-S (Nanoscribe GmbH) and a 25× objective lens (numerical aperture NA = 0.8, Carl Zeiss).

Uniaxial loading experiments. The uniaxial loading experiments are performed with the same setup that we have used previously[2], except that we have exchanged the force cell to a new one (K3D40 ± 2N, ME-Messsysteme, Germany). In this setup, a flat metal stamp in contact with the top of the metamaterial sample and moving along the z-direction contracts the sample. To control the process, we optically image the sample from the side and from the bottom. The axial strain of the sample is computed from the displacement u_z at the top of the sample via $\epsilon_{zz} = u_z/L_z$, that is, compression corresponds to $\epsilon_{zz} < 0$. Together with the handedness shown in Fig. 1, $\epsilon_{zz} < 0$ leads to $\varphi < 0$. The twist angle is obtained from digital image processing of the bottom images using image cross-correlation analysis[2,24,25] and averaging over the rotations obtained from the markers mentioned above (cf. Fig. 4). However, in contrast to our previous work (where we have fixed the sample side lengths L_x, L_y, and L_z, hence changed a when varying N), we here fix all lattice constants a_x, a_y, and a_z, and change the side lengths L_x, L_y, and L_z when varying N.

Data availability

The data that support the findings of this study are available from the corresponding author upon reasonable request and are published on the open access data repository of the Karlsruhe Institute of Technology (https://doi.org/10.5445/IR/1000126087).

Code availability

The code for simulation that support the findings of this study are available from the corresponding author upon reasonable request and are published on the open access data repository of the Karlsruhe Institute of Technology (KITopen).

References

1. Sommerfeld, A. *Mechanics of Deformable Bodies: Lectures on Theoretical Physics* Vol. 2 (Elsevier, 2016).
2. Frenzel, T., Kadic, M. & Wegener, M. Three-dimensional mechanical metamaterials with a twist. *Science* **358**, 1072–1074 (2017).
3. Coulais, C. As the extension, so the twist. *Science* **358**, 994–995 (2017).
4. Fernandez-Corbaton, I. et al. New twists of 3d chiral metamaterials. *Adv. Mater.* **31**, 1807742 (2019).
5. Chen, W. & Huang, X. Topological design of 3D chiral metamaterials based on couple-stress homogenization. *J. Mech. Phys. Solids* **131**, 372–386 (2019).
6. Ziemke, P., Frenzel, T., Wegener, M. & Gumbsch, P. Tailoring the characteristic length scale of 3d chiral mechanical metamaterials. *Extreme Mech. Lett.* **32**, 100553 (2019).
7. Zhong, R., Fu, M., Chen, X., Zheng, B. & Hu, L. A novel three-dimensional mechanical metamaterial with compression-torsion properties. *Compos. Struct.* **226**, 111232 (2019).
8. Wang, L. & Liu, H.-T. 3D compression-torsion cubic mechanical metamaterial with double inclined rods. *Extreme Mech. Lett.* **37**, 100706 (2020).
9. Ha, C. S., Plesha, M. E. & Lakes, R. S. Chiral three-dimensional isotropic lattices with negative poisson's ratio. *Phys. Status Solidi B* **253**, 1243–1251 (2016).
10. Eringen, A. C. *Microcontinuum Field Theories: I. Foundations and Solids* (Springer Science & Business Media, 2012).
11. Lakes, R. S. & Benedict, R. L. Noncentrosymmetry in micropolar elasticity. *Int. J. Eng. Sci.* **20**, 1161–1167 (1982).
12. Coulais, C., Kettenis, C. & van Hecke, M. A characteristic length scale causes anomalous size effects and boundary programmability in mechanical metamaterials. *Nat. Phys.* **14**, 40 (2018).
13. Kadic, M., Frenzel, T. & Wegener, M. Mechanical metamaterials: when size matters. *Nat. Phys.* **14**, 8 (2018).
14. Kadic, M., Diatta, A., Frenzel, T., Guenneau, S. & Wegener, M. Static chiral willis continuum mechanics for three-dimensional chiral mechanical metamaterials. *Phys. Rev. B* **99**, 214101 (2019).
15. Köpfler, J., Frenzel, T., Kadic, M., Schmalian, J. & Wegener, M. Topologically protected twist edge states for a resonant mechanical laser-beam scanner. *Phys. Rev. Appl.* **11**, 034059 (2019).
16. Timošenko, S. P. & Goodier, J. N. *Theory of Elasticity* 3rd edn (McGraw-Hill, Singapore, 1970).

17. Kadic, M., Milton, G. W., van Hecke, M. & Wegener, M. 3D metamaterials. *Nat. Rev. Phys.* **1**, 198–210 (2019).
18. Chen, Y., Frenzel, T., Guenneau, S., Kadic, M. & Wegener, M. Mapping acoustical activity in 3D chiral mechanical metamaterials onto micropolar continuum elasticity. *J. Mech. Phys. Solids* **137**, 103877 (2020).
19. Duan, S., Wen, W. & Fang, D. A predictive micropolar continuum model for a novel three-dimensional chiral lattice with size effect and tension-twist coupling behavior. *J. Mech. Phys. Solids* **121**, 23–46 (2018).
20. Hahn, V. et al. Rapid assembly of small materials building blocks (voxels) into large functional 3D metamaterials. *Adv. Funct. Mater.* **30**, 1907795 (2019).
21. Frenzel, T., Köpfler, J., Jung, E., Kadic, M. & Wegener, M. Ultrasound experiments on acoustical activity in chiral mechanical metamaterials. *Nat. Commun.* **10**, 1–6 (2019).
22. Bückmann, T. et al. Tailored 3D mechanical metamaterials made by dip-in direct-laser-writing optical lithography. *Adv. Mater.* **24**, 2710–2714 (2012).
23. Kong, L. & Cui, M. A high throughput (>90%), large compensation range, single-prism femtosecond pulse compressor. arXiv:1306.5011. Preprint at https://arxiv.org/pdf/1306.5011 (2013).
24. Bückmann, T., Thiel, M., Kadic, M., Schittny, R. & Wegener, M. An elasto-mechanical unfeelability cloak made of pentamode metamaterials. *Nat. Commun.* **5**, 4130 (2014).
25. Eberl, C., Gianola, D. & Bundschuh, S. Free digital image correlation and tracking functions. https://www.mathworks.com/matlabcentral/fileexchange/12413 (2010).

Acknowledgements

Author contributions

T.F., V.H., and P.Z. contributed equally to this work. M.W. and P.G. supervised the work. T.F., P.Z., P.G., and M.W. conceived the experiments. T.F. and P.Z. designed the unit cell. T.F. and M.W. proposed the simple analytical model. T.F. and P.Z. performed the finite element microstructure calculations. P.Z. developed and performed the finite element microstructure calculations using the Timoshenko beam approximation. P.Z. and Y.C. implemented and performed the micropolar continuum simulations. V.H. and P.K. built the multi-focus multi-photon 3D printer. T.F., V.H., and J.L.G.S. fabricated the samples. T.F. and J.L.G.S. conducted the experiments. All authors discussed the results. M.W. wrote a first draft of the paper. All authors contributed to the final version of the paper.

Funding

Competing interests

The authors declare no competing interests.

Additional information

Supplementary information is available for this paper at https://doi.org/10.1038/s43246-020-00107-w.

Correspondence and requests for materials should be addressed to M.W.

Peer review information Primary handling editor: Aldo Isidori.

Reprints and permission information is available at http://www.nature.com/reprints

Publisher's note Springer Nature remains neutral with regard to jurisdictional claims in published maps and institutional affiliations.